Energy Harvesting and Remote Powering for Implantable Biosensors

Jacopo Olivo, Sandro Carrara, *Member, IEEE,* and Giovanni De Micheli, *Fellow, IEEE*

***Abstract*—The paper reviews some popular techniques to harvest energy for implantable biosensors. For each technique, the advantages and drawbacks are discussed. Emphasis is placed to the inductive links, able to deliver power wirelessly through the biological tissues and to enable a bidirectional data communication with the implanted sensors. Finally, high frequency inductive links are described, focusing also on the power absorbed by the tissues.**

***Index Terms*—Energy harvesting, remote powering, implantable biosensors, inductive powering.**

I. Introduction

Nowadays there is an increasing interest in the field of implantable biosensors. The possibility of real-time monitoring of the human body from inside paves the way to a great number of applications and offers wide scenarios for the future.

A promising application is the use of implanted electrode arrays to monitor local neural circuits and the related spiking activity [1–4]. The study of brain neural activity is a great help in the treatment of disorders such as blindness, deafness, epilepsy, Parkinson's disease and paralysis. For instance, in the latter mentioned disorder, by observing the emission rate of electrical impulses occurring when particular movements are done, it is possible to transform these signals in commands for neuro-prosthetic devices. These devices, controlled directly by the thought through the nerve signals [5], are thus able to partially render the mobility to people with motion disabilities.

The brain is not the only application area for implantable biosensors; significant effort is dedicated to the design and development of implantable chemical sensors, capable to detect the concentration of clinically relevant species [6] or to constantly monitor the health status by collecting biometric data to better calibrate a therapy or to prevent dangerous events, such as hearth attacks or ictus.

Several key challenges must be addressed to realize these scenarios: implantable biosensors should be minimally invasive, completely biocompatible, with a low thermal dissipation [7], and a large power autonomy. In particular, this latter aspect must be carefully considered, since the performance of an implanted device depends on the power availability.

Modern batteries have increased capabilities with respect to those available in the past: for example, lithium-ion batteries have reached a high level of energy density (up to $0.2\ \mathrm{Wh/g}$) and are able to maintain an almost constant voltage until they are discharged to 75%-80% [8]. Unfortunately, size constraints of implantable batteries limit their efficiency and their repeated use implies their substitution after a while.

J. Olivo, S. Carrara and Giovanni De Micheli are with the Integrated Systems Laboratory, EPFL - École Polytechnique Fédérale de Lausanne, Lausanne, Switzerland (e-mail: jacopo.olivo@epfl.ch).

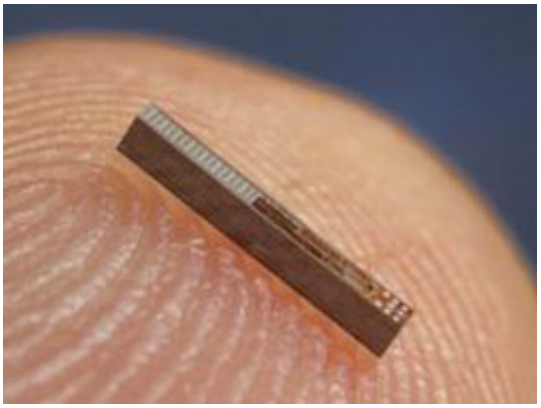

Fig. 1. Implantable sensor, having 1-mm diameter, to measure and monitor blood pressure. Image from [9].

Power constraints can be relaxed by energy harvesters, also named energy scavengers. These devices exploit natural or artificial power sources surrounding the person to assist the implanted batteries, to recharge them and in certain cases even to replace them. Energy harvesters for implantable biosensors have been exhaustively studied and a large number of solutions for different cases can be found in literature.

Most of the physical phenomena have been studied to obtain harvesters suitable for in-body applications, having minimum invasivity and high efficiency. This paper aims at reviewing some of these solutions, discussing the pros and cons, the related applications and the potential of each solution. The paper is organized as follows. Section 2 discusses some of the most popular harvesting techniques for on-body and in-body applications. Section 3 describes in detail the use of inductive links for wireless remote powering of implanted devices. Finally, Section 4 concludes the paper. In the Appendix is provided a brief introduction to the study of inductive links by means of the scattering parameters.

II. Harvesting and Remote Powering Techniques

In this section, some of the most popular harvesting techniques for implantable biosensors are discussed, presenting for each technique the advantages and the disadvantages. The last paragraph of this section offers an outlook of some new emerging techniques inspired by the biological mechanisms.

A. Kinetic

Kinetic harvesters aim to collect the energy related to human motions and transform it into electrical energy [10]. This kind of harvesters can be classified into three categories, depending on the employed transduction method: electromagnetic, electrostatic, and piezoelectric.

Kinetic harvesters using electromagnetic transducers are able to generate an electromotive force due to the change of an external magnetic flux through a closed circuit. The change of flux can be induced, for instance, by rotating the circuit along an axis, thereby changing the surface associated to the magnetic flux.
This method has been used by Seiko to power the quartz wristwatch "Seiko Kinetic" [11]. This watch is able to self-charge by the means of wrist motion, transmitted by an oscillating weight to a magnetic rotor linked to a coil [12]. The motion of the rotor induces an electromotive force through a coil and the generated charge is stored in a common battery. Moreover, this harvester is equipped with a charge pump circuit with different multiplicative factors to quickly increase the voltage of the battery, in order to reduce as much as possible the start-up time of the watch.
The approach of Seiko has been successfully tested also in biomedical field, being able to exploit the heart beats to charge a pacemaker battery [13]. Implanted on a dog, this energy harvester has collected $80\ \mathrm{mJ}$ after $30\ \mathrm{minute}$ with a cardiac frequency of about 200 beats per minute: around $13\ \mu\mathrm{J}$ per beat with a returned power of about $44\ \mu\mathrm{W}$. A possible drawback of this technique is the necessity to periodically lubricate the moving parts, which in the end need to be replaced when worn out. Moreover, the size of the oscillating weight makes this solution not suitable for low invasive biosensors with small dimensions.

Kinetic harvesters based on electrostatic transducers utilize variable capacitors having the position of the plates changed by an external force. They can work with fixed charge or with fixed voltage. Working with fixed charge, the external force changes the voltage across the capacitor, while working with fixed potential the motion of the plates generates current through the capacitor. Independently by the operation mode, in most of the cases they need to be precharged to operate. This technique has a low efficiency when high power is required, but works quite well with devices having low power requirements, such as the implantable biosensors. Furthermore, it is appropriate for MEMS realization.
The literature offers kinetic harvesters with electrostatic transducers that can render up to $58\ \mu\mathrm{W}$ when set in motion by a force emulating the cardiac signal, exploiting a capacitor with a capacitance variable between $32\ \mathrm{nF}$ and $110\ \mathrm{nF}$ [14]. A MEMS electrostatic harvester rendering $80\ \mu\mathrm{W}$ when excited with an acceleration of $10\ \mathrm{m/s^2}$ has been proposed [15]. This harvester is dedicated to biomedical applications and operates with constant charge; moreover it is non-resonant, thus it can operate over a wide range of oscillation frequencies.

Finally, the kinetic harvesters based on piezoelectric transducers use the capability of the piezoelectric materials to generate an electric field when subjected to a mechanical deformation. Differently from the electrostatic transducers, no precharging is required. Piezoelectric harvesters based on *Aluminum Nitride* (AIN) have returned up to $60\ \mu\mathrm{W}$, with a footprint smaller than $1\ \mathrm{cm^2}$ [16]; this power, however, is obtained with unpackaged devices and could significantly decrease once the harvesters are packaged; Piezoelectric harvesters based on *Lead Zirconate Titanate* (PZT) have obtained up to $40\ \mu\mathrm{W}$ [17].

Kinetic harvesters are widely used in commercial sensors available in the market. $\mathrm{Perpetuum}^{©}$ [18] and $\mathrm{EnOcean}^{©}$ [19] provide a large spectrum of solutions for different application fields, including wireless sensor nodes. None of these commercial solutions is however dedicated to implantable biosensors.

B. Thermoelectric Effect

Scavengers exploiting thermal gradients to generate energy are based on the Seebeck effect. Due to a temperature difference between two different metals or semiconductors, a voltage drop is created across them.

The core element of this kind of scavengers is the thermocouple (Fig. 2): two materials are linked together maintaining their junctions at different temperatures. The voltage generated across a thermocouple due to a temperature difference $(T_1 - T_2)$ can be expressed as,

$$V = \int_{T_1}^{T_2} [S_{\mathrm{B}}(T) - S_{\mathrm{A}}(T)]\mathrm{d}T\ , \tag{1}$$

where S_{A} and S_{B} are the thermoelectric powers (or Seebeck coefficients) of the two materials A and B. Semiconductors typically have a high Seebeck coefficient and that is why these materials are commonly used for thermocouples; moreover, *n*-type and *p*-type semiconductors have Seebeck coefficients with different signs, so that if the two semiconductors composing a thermocouple have opposite doping the contributions to the voltage reported in (1) are summed.

Energy scavengers exploiting the thermoelectrical effect consist of many thermocouples connected electrically in series and thermally in parallel to create a thermopile (Fig. 3). Additional elements, such as radiators and structures to convey the heat into the thermopile legs are normally used to increase the efficiency of such devices.

Thermopiles are usually inserted in a thermal circuit as depicted in Fig. 4. If we assume that the thermopile is placed between the human body (source) and the external

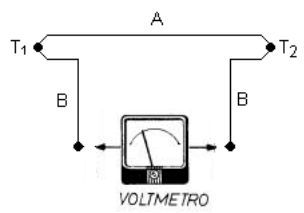

Fig. 2. Schematic representation of a thermocouple: two different materials are linked together keeping their junctions at different temperatures. A voltage drop is thus created across them because of the Seebeck effect.

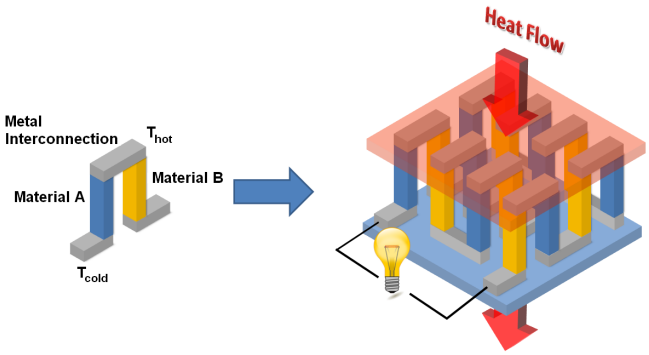

Fig. 3. The connection of many thermocouples (left) electrically in series and thermally in parallel forms a thermopile (right).

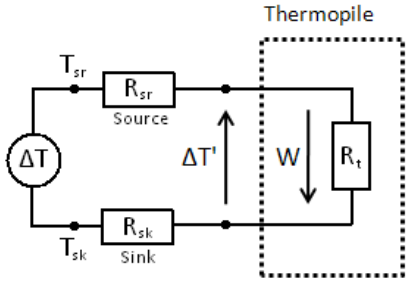

Fig. 4. Schematic example of a thermal circuit.

ambient (sink), R_{sr} represents the thermal resistance during heat exchange between hot plate of the thermopile and the body, while R_{sk} represents the thermal resistance during heat exchange between cold plate of the thermopile and the ambient. The temperature difference between the body and the ambient is denoted as ΔT, while $\Delta T'$ is the temperature difference effectively present across the thermopile plates. The thermopile has a thermal resistance between the plates equal to R_{t} and a heat flux W flows across it. In this description, the heat flux is considered constant: this assumption remains valid only for high values of the thermal resistances R_{sr} and R_{sk}.

The thermal resistance R_{t} of the thermopile is the parallel combination of the thermal resistance R_{p} of the thermopile legs, also called pillars, and the thermal resistance R_{a} of the air in between the legs.

$$\begin{cases} R_{\mathrm{p}} = \dfrac{h}{2na^2} r_{\mathrm{p}} \ , & \text{(2a)} \\ R_{\mathrm{a}} = \dfrac{h}{A - 2na^2} r_{\mathrm{a}} \ , & \text{(2b)} \end{cases}$$

where A is the area of the thermopile plates, h is the height of the pillars, equal to the distance between the plates, a is the lateral dimension of the pillars, assumed with square base. The parameter n represents the number of thermocouples (each one having 2 pillars) while r_{a} and r_{p} are the thermal resistivity of the air and of the pillars, respectively.

It is possible to demonstrate that R_{p} and R_{a} should be equal to maximize the generated power. Thus, by equalizing the two previous expressions the optimum number of thermocouples to be used in a thermopile is obtained:

$$n = \frac{r_{\mathrm{p}}}{r_{\mathrm{p}} + r_{\mathrm{a}}} \cdot \frac{A}{2a^2} = \frac{r_{\mathrm{p}}}{R_{\mathrm{a}}} \cdot \frac{h}{2a^2} \ . \tag{3}$$

The thermal gradient $\Delta T'$ across the thermopile can be written as

$$\Delta T' = W R_{\mathrm{t}} = W \frac{R_{\mathrm{p}}}{2} \ , \tag{4}$$

where the thermal resistance of the thermocouple R_{t} is the parallel of R_{p} and R_{a}. R_{p} has been fixed equal to R_{a} to maximize the generated power.

The electrical parameters of the thermopile can be determined as

$$\begin{cases} \Delta V = n S_{\mathrm{p}} \Delta T' = r_{\mathrm{p}} \dfrac{S_{\mathrm{p}} W}{4} \cdot \dfrac{h}{a^2} \ , & \text{(5a)} \\ R = 2n\rho \dfrac{h}{a^2} = \dfrac{r_{\mathrm{p}}}{r_{\mathrm{p}} + r_{\mathrm{a}}} \cdot \dfrac{\rho A}{h} \cdot (\dfrac{h}{a^2})^2 \ . & \text{(5b)} \end{cases}$$

The equation (5a) returns the voltage drop across the entire thermopile and is obtained from (1) considering S_p the sum of the Seebeck coefficients of the two pillars of every thermocouple. The equation (5b) describes the electrical resistance R of the thermopile, where ρ is the electrical resistivity of the pillars.

Finally, the power delivered by the thermopile to a matched load is equal to

$$P = \frac{\Delta V^2}{4R} = \frac{1}{64} \frac{S_{\mathrm{p}}^2 W_{\mathrm{u}}^2 A h}{\rho} (r_{\mathrm{p}} + r_{\mathrm{a}}) r_{\mathrm{p}} \ , \tag{6}$$

where $W_{\mathrm{u}} = W/A$ is the heat flux per unit area. A common figure of merit for the thermopiles is the following

$$\mathrm{ZT} = \frac{S_{\mathrm{p}}^2 r_{\mathrm{p}}}{\rho} \Delta T' \ . \tag{7}$$

ZT is a dimensionless factor describing the performance of a thermocouple.

By the formulas just introduced the voltage V is shown to be proportional to h/a^2, while the power P is proportional to h. The aspect h/a between the height of the pillars and the lateral dimension is limited by technology aspects [20]. Thus, by increasing h to obtain a higher power, h/a^2 is decreased and, hence, the voltage. For this reason there is no space for simultaneously optimizing of power and voltage.

When low thermal gradients are applied, as in the case of human body applications, to obtain voltage levels useful to power integrated circuitry is not straightforward. Commercial thermopiles commonly use bismuth telluride (Bi_2Te_3), having Seebeck coefficient $S = \pm 0.2\ \mathrm{mV/^\circ C}$, due to the high ZT factor. By using that material for the thermocouple pillars, with a temperature difference $\Delta T' = 1\ ^\circ\mathrm{C}$, 5000 thermocouples having a total area of about $25\ \mathrm{cm}^2$ are required to produce a voltage drop $\Delta V = 1\ \mathrm{V}$ [21].

Moreover, a value of $\Delta T' = 1\ ^\circ\mathrm{C}$ between the thermopile plates is not easily achieved. Based on results from [21], placing a commercial thermopile exploiting bismuth telluride on a human forearm and considering an area $A = 1\ \mathrm{cm}^2$, we can

TABLE I
HUMAN TEMPERATURE GRADIENTS AT ROOM TEMPERATURE. TABLE FROM [22].

Site	Muscle Thickness (mm)	Fat Thickness (mm)	Rested (v=0.2 m/s) ΔT(K)	Walking (v=1.56 m/s) ΔT(K)	Running (v=4.25 m/s) ΔT(K)
Abdomen	16.34	14.8	1.73	3.8	4.75
Biceps	34.6	3.33	0.45	1.22	1.7
Calf-posterior	65.36	4.93	0.65	1.74	2.4
Chest	33.45	7.26	0.94	2.37	3.18
Forearm	26.04	3.24	0.44	1.16	1.63
Hamstring	69.29	6.97	0.91	2.32	3.14
Lumbar	37	6.54	0.85	2.18	2.96
Quadriceps	54.54	6.42	0.82	2.12	2.89
Subscapular	23.74	8.4	1.06	2.6	3.44
Suprapatellar	29.42	6.23	0.81	2.08	2.81
Triceps	41.84	5.92	0.78	2.02	2.75

assume as reasonable the following values: $R_{\mathrm{sr}} = 500\ \mathrm{K/W}$, $R_{\mathrm{sk}} = 1030\ \mathrm{K/W}$, $R_{\mathrm{t}} = 50\ \mathrm{K/W}$, $T_{\mathrm{sr}} = 37.5\ ^{\circ}\mathrm{C}$, $T_{\mathrm{sk}} = 28\ ^{\circ}\mathrm{C}$. If the heat flux W passing through the thermopile is

$$W = \frac{\Delta T}{(R_{\mathrm{sr}} + R_{\mathrm{sk}} + R_{\mathrm{t}})}\ , \tag{8}$$

a heat flux of about $W = 6\ \mathrm{mW}$ flows through the area A. The product of the heat flux by the thermal resistance of the thermopile results in temperature gradient $\Delta T' = 0.3\ ^{\circ}\mathrm{C}$, instead of $1\ ^{\circ}\mathrm{C}$ previously assumed. With this value of $\Delta T'$, the thermopile area must be increased up to $83\ \mathrm{cm}^2$ to obtain a voltage drop of $\Delta V = 1\ \mathrm{V}$, making impractical any kind of implant application. In order to compare the different implantation areas, Table I from [22] shows the calculated temperature gradients present in different parts of the human body, with an ambient temperature of $25\ ^{\circ}\mathrm{C}$.

Charge pumps are commonly used to elevate the voltage drops generated by the thermocouples, thus overcoming the problems related to the low voltages generated by the thermal scavengers [23–26]. Seiko proposed a thermoelectric wristwatch where a voltage of about $300\ \mathrm{mV}$ is boosted until $1.5\ \mathrm{V}$, a useful level to power the $1\ \mu\mathrm{W}$ quartz circuit [27]. The whole scavenger can provide a total power of $22.5\ \mu\mathrm{W}$.

The literature offers some examples of thermopiles exploiting the human warmth and a considerable effort has been invested to improve the technology performance of such systems. However, the power range of thermoelectric harvesters when exploiting the human warmth is still quite low and generally it does not exceed the few hundreds of $\mu\mathrm{W}$ when thermal difference below $5\ \mathrm{K}$ are applied. In [28] $1.5\ \mu\mathrm{W}$ with a $0.19\ \mathrm{cm}^3$ device exploiting a thermal gradient of $5\ \mathrm{K}$ is obtained. Similar results have been obtained by [29] with a device able to return $1\ \mu\mathrm{W}$ with an area of $1\ \mathrm{cm}^2$ and a thermal gradient of $5\ \mathrm{K}$. ThermoLife [30] proposes a commercially available solution able to produce up to $30\ \mu\mathrm{W}$ ($10\ \mu\mathrm{A}$ with a voltage drop of $3\ \mathrm{V}$) when a temperature difference of $5\ \mathrm{K}$ is applied. This device has a volume of $95\ \mathrm{mm}^3$ and a weight of $0.23\ \mathrm{g}$.

C. Fuel Cells

A fuel cell is an electrochemical device that generates current through the reaction of two chemical species flowing into it, the fuel on the anode site and the oxidant on the cathode site. The main difference between a fuel cell and a traditional battery is that the former one can produce energy virtually without stopping, as long as the reactants continue to be present.

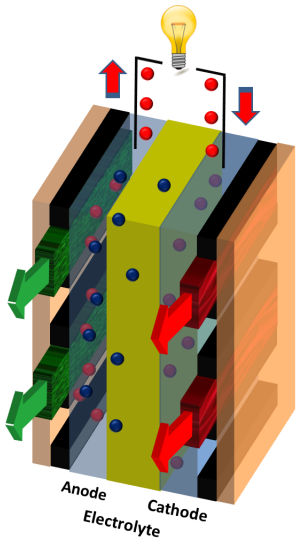

Fig. 5. Schematic description of a PEM fuel cell. Electrons cannot cross the membrane, thus they have to follow a different path, generating current.

Fuel cells exist in many different kinds. The most common is the *Proton Exchange Membrane* (PEM) fuel cell (Fig. 5). The fuel and the oxidant streams are separated by a membrane that allows only protons produced on the anode site to cross it and to reduce the oxidant on the cathode site. The electrons generated on the anode cannot pass directly through the membrane to reach the cathode, consequently they have to follow a different external path, generating current.

Recently, a new kind of membrane-less fuel cells has been introduced [31, 32]. They exploit the laminar characteristics of micro-channel flows to keep the two reactants separated, avoiding in this way the use of a membrane. Indeed, the PEM membrane needs a constant humidification and it is subject to degradation and fuel crossover. In addiction, the cost is usually quite high. Membrane-less fuel cells, instead, are more compact and enable a significant miniaturization. Additionally, they do not require water management or cooling system. A schematic example of a membrane-less fuel cell is reported in Fig. 6.

The use of fuel cells exploiting species present into the human body to harvest energy for implantable biosensors offers considerable advantages. The constant presence and availability of the reactants directly into the body makes unnecessary external recharging mechanisms or replacement. Implantable fuel cells using glucose as reactant are probably the most studied biofuel cells, due to the high availability of glucose in body fluids. Note that the investigation and development of such cells have started since the 1960's [33].

Glucose fuel cells can be divided into two groups: *abiotically catalyzed* and *enzymatically catalyzed*. The former group utilizes non-biological catalysts, such as noble metals or activated carbon. The latter group, instead, uses enzymes,

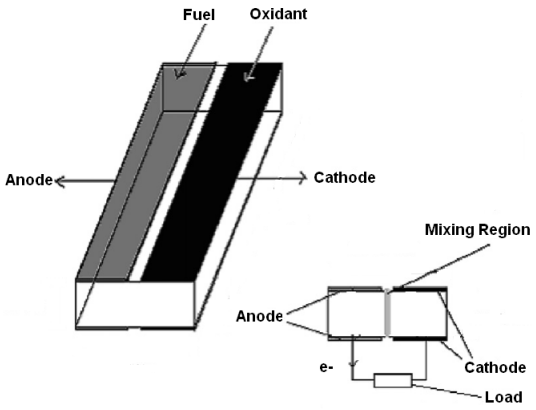

Fig. 6. Schematic description of a membrane-less fuel cell. The laminar characteristics of micro-channel flows are used to keep reactants separated. Image elaborated from [39].

such as glucose oxidase or laccase, as catalysts to enable the electrode reactions. In [34] the state of the art of these devices is reported. During *in vitro* experiments glucose fuel cells abiotically catalyzed can generate up to $50\ \mu\mathrm{W/cm^2}$ [35]. Experiments *in vivo* performed on a dog have generated $2.2\ \mu\mathrm{W/cm^2}$ over a period of 30 days [36]. Enzymatically catalyzed cells can provide a higher power density, up to $430\ \mu\mathrm{W/cm^2}$ [37]. Unfortunately, the lifetime of their enzymatic catalyst has been not proved beyond a period of one month [38].

D. Infrared Radiation

This kind of harvesters exploits an external infrared source to transmit power to an implanted photodiode array; this latter converts the received radiation into a current to properly charge the sensor battery (Fig. 7).

Some examples about this typology of scavengers are discussed in [40, 41]. The device presented in [41] can supply power in the order of hundreds μW up to few mW when illuminated by a power density of some $\mathrm{mW/cm^2}$. The power returned by that photodiode array when enlighten by a power density of $22\ \mathrm{mW/cm^2}$ for $17\ \mathrm{min}$ is sufficient to allow a $20\ \mu\mathrm{A}$ cardiac pacemaker to operate for $24\ \mathrm{h}$. In terms of power, it means about $4\ \mathrm{mW}$ of transmitted power if the voltage of the pacemaker battery is considered equal to $2.4\ \mathrm{V}$, an average value between the nominal operating voltage ($2.8\ \mathrm{V}$) and the minimum operating voltage ($2.0\ \mathrm{V}$). This result has been obtained with a skin temperature rise of $1.4\ ^\circ\mathrm{C}$, a safe value for this kind of tissue [42].

This performance has been achieved by means of a large photodiode array, having an area of $2.1\ \mathrm{cm^2}$ and placed in a subcutaneous zone extremely near to the infrared emitter ($0.8\ \mathrm{mm}$). To obtain the same performance without a further temperature increase when a thicker tissue is used, the array dimensions can be enlarged. In [41] the same results are demonstrated where a $2\ \mathrm{mm}$ human skin is used as barrier with a $10\ \mathrm{cm^2}$ photodiode array. Finally, to increase the emitter power densities to reduce the photodiode area is not recommended. Most of the heat generated by these scavengers is due to the array heating and a smaller array receiving a greater power density would involve a considerable temperature rise in the implantation zone.

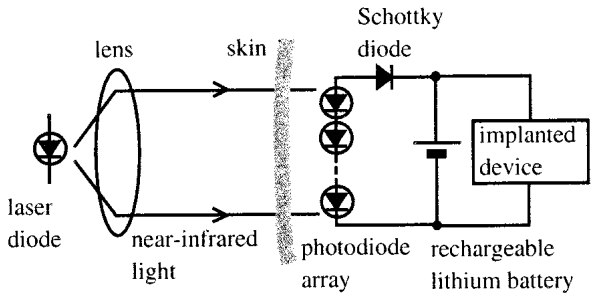

Fig. 7. Example of an infrared harvester. The infrared light emitted by an external source is caught by an implanted photodiode array. Image from [41].

Due to the area constrains and the difficulties to operate with tissues having high thickness, this kind of harvesters is suitable for large devices not deeply implanted (i.e. cardiac pacemakers) but is practically ineffective with less invasive, deeply implanted devices.

E. Low Frequency Magnetic Fields

This kind of harvesters uses low frequency magnetic fields placed outside the body to move an implanted magnetic rotor and to generate power exploiting its mechanical rotation (Fig. 8). Some solutions using this technique have been reported in literature [43, 44].

One of the advantages in employing this kind of scavengers is the high quantity of power that they can deliver over a relatively big distance and even to deeply implanted biosensors. A maximum power of $3.1\ \mathrm{W}$ over a distance of $1.5\ \mathrm{cm}$ has been reported by [43], with an attractive force between the external and the internal rotors of $1.6\ \mathrm{N}$. This value has been obtained with a speed of the internal rotor of about $547\ \mathrm{rad/s}$. At a lower speed, up to $0.2\ \mathrm{W}$ can be delivered over a distance of $2\ \mathrm{cm}$ when the implanted rotor is rotating at $273\ \mathrm{rad/s}$ and the resistance of the load is $200\ \Omega$.

The major drawback of this technique is the large dimension of the implanted rotor, about $10\ \mathrm{cm^3}$. This volume hinders the implantation process. Moreover, moving components need to be periodically lubricated and substituted when worn out.

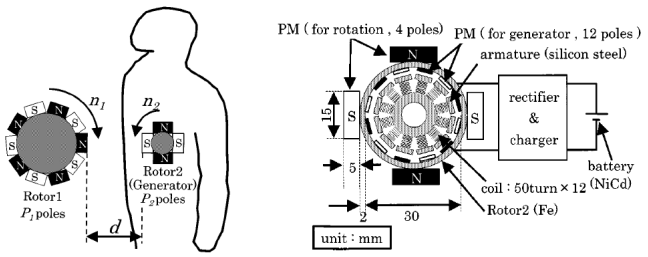

Fig. 8. Low frequency magnetic fields are used to move an implanted rotor to generate power. Images elaborated from [43].

F. Inductive Links

The use of inductive links to power implanted sensors has been deeply investigated in the last decade. An inductive link consists of two coils. The primary coil is placed outside the body, generating a variable magnetic field by means of an alternate current flowing in it. The change of the magnetic flux through the secondary coil generates across it an electromotive force, according to the Faraday-Neumann-Lenz law

$$\varepsilon = -\frac{\mathrm{d}\phi_{\mathrm{B}}}{\mathrm{d}t} \ , \tag{9}$$

where ε is the electromotive force generated by the change of the magnetic flux ϕ_{B} through the secondary coil. The minus sign in the right side of the equation indicates that the generated electromotive force opposes the flux change. Using this method, power is transferred wirelessly through the body tissues, inducing an electromotive force in the implanted coil by means of an alternate current flowing on the external coil.

Inductive links present considerable additions, when compared with other kinds of power transmission previously discussed. Exploiting this technique, data can be transmitted from outside to inside the body (*downlink*) and vice versa (*uplink*) without using a radio-frequency transmitter or receiver (Fig. 9). This can be feasible by modulating the load of the secondary coil, varying in this way the total load seen by the primary coil. This technique of data transmission, often named *backscattering*, allows to save a large amount of energy by avoiding the use of an implanted RF transmitter. Indeed, the RF transmitter usually has the highest power consumption among the components of an implantable biosensor. The capability to avoid an implanted RF transmitter, together with a delivered power up to few mW, make this technique particularly suitable for low-invasive implantable biosensors. Many applications, involving inductive harvesting techniques, have been reported in literature. Such solutions are discussed in detail in the following section, preceded by a brief theoretical introduction.

Such technique presents strong analogies with the use of RFID passive tags [45]. An RFID passive tag consists of an integrated circuit with memory that is powered by the incidental field generated by a reader. Once powered, the chip generally transmits its identification tag to the reader by means of an RF transmitter or by exploiting the backscattering technique. Thus, an RFID passive tag needs energy only when the tag is required by the reader and it is not equipped with a battery. Implantable biosensors, instead, could need to be powered even when no reading occurs. Thus, in most cases the biosensors must be equipped with an implanted battery.

In the market commercial products exploiting inductive links to power fully implanted biosensors are available. One of these products is the neurostimulator "RestoreUltra" produced by Medtronic [46]. It is a stimulator of the spinal cord and is equipped with a battery that can be recharged from outside avoiding invasive surgeries.

G. Emerging Techniques

The biological processes in animals and plants to collect, store and reuse energy can inspire novel harvesting techniques.

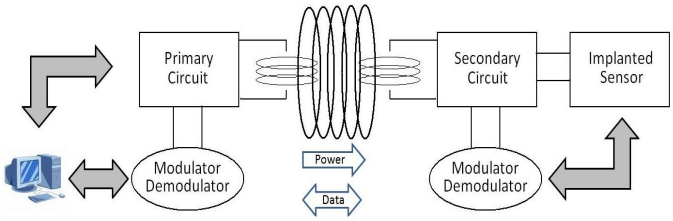

Fig. 9. Schematic representation of an inductive powering performing bidirectional data transmission.

Some works have presented strong analogies between complex electronic systems and biological energy management [47].

For example, natural photosynthesis permits plants to collect energy by exploiting the solar light as source and CO_2 and water as reactants. Several efforts have been invested to artificially reproduce the key steps of the photosynthesis, in order to generate electrical power and energy fuels [48, 49]. Ref. [50] has proposed a photosynthetic light conversion unit that mimics the light-harvesting structure of phototrophic bacteria. An array of self-assembled bacteriochlorophyll aggregates captures and conveys the solar energy to an embedded "reaction center". This latter has the role of energy acceptor and contributes to the charge transfer.

Another kind of scavenger inspired by the natural photosynthesis is the Gräetzel's cell or *dye-sensitized solar cell* (DSSC) [51]. This device has two electrodes, one of which is transparent to the solar light. In between the two electrodes, a molecular dye converts the solar light in electrons that reach the anode electrode by means of a stratum of titanium dioxide (TiO_2). The electron holes generated into the dye reach the cathode electrode through a liquid electrolyte. The whole mechanism is similar to the natural photosynthesis. Indeed, in this approach the dye has the same role of the chlorophyll (conversion of light in electrons), the electrolyte has the same role of the water (replacement of the generated electrons), and the TiO_2 has the same role of the CO_2 (electrons acceptor).

This harvesting technique, although at the moment is not directly applicable to the field of the implantable biosensors, could be used in the near future to power devices not deeply implanted. A possible target, for example, could be subcutaneous biosensors due to their proximity to the skin and to the solar light.

III. Inductive Links for Remote Powering of Implanted Biosensors

A. Introduction

As aforementioned, inductive links are a well-suited solution for implanted biosensors due to the possibility to perform a bidirectional communication between the internal sensor and the external control devices. Furthermore, the low dimension makes them compatible with low-invasive body implantations.

Almost all the works reported in the literature utilize frequencies in the order of few MHz or lower [52–60]. The reason behind this choice is that this range of frequencies minimizes the power absorption by the tissues, yielding a higher transmission efficiency. At these frequencies, an inductive link can

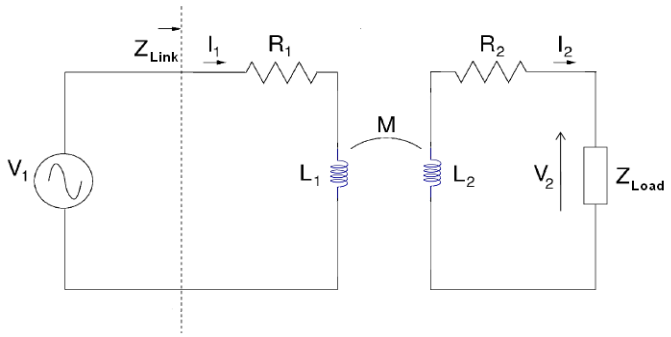

Fig. 10. An inductive link is obtained with a primary coil L_1 connected to a power source and magnetically coupled to a secondary coil L_2.

be analyzed by means of the Kirchhoff's laws using lumped parameters [61].

An example of an inductive link is illustrated in Fig. 10. The behavior of that circuit is described, according to (9), by the following formulas

$$\begin{cases} V_1 = +R_1 I_1 + \dfrac{\mathrm{d}\phi_1}{\mathrm{d}t} \ , & \text{(10a)} \\ V_2 = -R_2 I_2 - \dfrac{\mathrm{d}\phi_2}{\mathrm{d}t} \ , & \text{(10b)} \end{cases}$$

where R_1 and R_2 represent the parasitic resistances of the two coils, ϕ_1 is the total magnetic flux through the primary coil and ϕ_2 is the total magnetic flux through the secondary coil. The voltages and the currents reported in (10) are functions of time.

Defining the self-inductances L_1 and L_2 of the two coils and their mutual inductance M as

$$\begin{cases} L_1 = \dfrac{\partial \phi_1}{\partial I_1} \ , & \text{(11a)} \\ L_2 = \dfrac{\partial \phi_2}{\partial I_2} \ , & \text{(11b)} \\ M = \dfrac{\partial \phi_1}{\partial I_2} = \dfrac{\partial \phi_2}{\partial I_2} \ , & \text{(11c)} \end{cases}$$

the expressions in (10) can be rewritten as

$$\begin{cases} V_1 = +R_1 I_1 + L_1 \dfrac{\mathrm{d}I_1}{\mathrm{d}t} - M \dfrac{\mathrm{d}I_2}{\mathrm{d}t} \ , & \text{(12a)} \\ V_2 = -R_2 I_2 - L_2 \dfrac{\mathrm{d}I_2}{\mathrm{d}t} + M \dfrac{\mathrm{d}I_1}{\mathrm{d}t} \ . & \text{(12b)} \end{cases}$$

The system can be finally described in the frequency domain by

$$\begin{cases} V_1 = +R_1 I_1 + j\omega L_1 I_1 - j\omega M I_2 \ , & \text{(13a)} \\ V_2 = -R_2 I_2 - j\omega L_2 I_2 + j\omega M I_1 \ , & \text{(13b)} \end{cases}$$

where V and I represent now complex phasors.

It is now possible to define some important parameters of the inductive links. First of all, we can express the voltage across the load as a function of the source voltage:

$$V_2 = \frac{j\omega M Z_{load}}{\omega^2 (M^2 - L_1 L_2) + j\omega (L_1 Z_{load} + L_1 R_2 + L_2 R_1) + R_1 Z_{load} + R_1 R_2} V_1 \ . \tag{14}$$

Since the complex power of a sinusoidal source V generating a current I can be defined as $P = \frac{VI^*}{2}$, the power transfer efficiency η of the link can be written as

$$\eta = \frac{\Re(V_2 I_2^*)}{\Re(V_1 I_1^*)} = \frac{\omega^2 M^2 R_{load}}{\omega^2 M^2 (R_2 + R_{load}) + R_1 [(R_2 + R_{load})^2 + (\omega L_2 + X_{load})^2]} \ . \tag{15}$$

where R_{load} and X_{load} are the real and the imaginary parts of Z_{load}, respectively.

Finally, the input impedance seen by the voltage source V_1 can be expressed as

$$Z_{link} = R_1 + j\omega L_1 + \frac{\omega^2 M^2}{R_2 + j\omega L_2 + Z_{load}} \ . \tag{16}$$

In most of the cases, the power signal driving the primary circuit is generated by a class-E amplifier, due to the higher efficiency of this circuit as compared to conventional class-B or class-C amplifiers [62].

Downlink transmission can be achieved by modulating the power signal generated by the class-E amplifier. *Amplitude Shift Keying* (ASK) is one of the most preferred modulation techniques, due to the simplicity of the demodulator that permits to reduce the area and the power consumption of the implanted chip. In addition, this kind of modulation enables a simple synchronization between transmitter and receiver. On the other hand, by modifying the amplitude of the power signal, the transmission efficiency becomes sub-optimal. Furthermore, the data transmission rate is lower as compared with other kinds of downlink modulations.

Another solution for the downlink communication is the *Frequency Shift Keying* (FSK). It permits to reach higher transmission rate if compared to the ASK, but this result is achieved by means of a more complex demodulator and by increasing the difficulty of synchronization between transmitter and receiver [63].

Uplink transmission is commonly achieved by means of the *Load Shift Keying* (LSK). By modifying the impedance $\mathrm{Z_{load}}$ of the secondary circuit, the load $\mathrm{Z_{link}}$ seen by the primary circuit consequently varies, causing the current flowing on the primary coil to change. This change can be detected by an external demodulator, enabling the uplink transmission without any internal RF transmitter.

B. High Frequency Inductive Links

As previously mentioned, almost all the works reported in the literature utilize frequencies in the order of few MHz or lower [52–60] since this range of frequencies minimizes the power absorbed by the tissues, yielding a higher transmission efficiency. A recent work [64] has questioned this choice: the tissue absorption increases with the frequency only if the displacement current is omitted into the Maxwell equations (*quasi-static assumption*). In that case, the propagation of the electromagnetic field is governed by a diffusion equation and decays exponentially inside the tissues. The diffusion length in that case is inversely proportional to the square root of the frequency. This approximation is valid with good conductors, but is not valid if the human body is modeled as a low loss dielectric. Without using the quasi-static assumption,

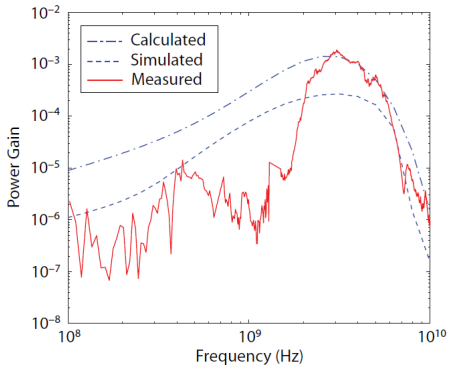

Fig. 11. Power gain obtained by [64] using an inductive link composed of two $4\ \mathrm{mm}^2$ coils. Simulations and measurements produce an optimal transmission frequency around 2.5 GHz.

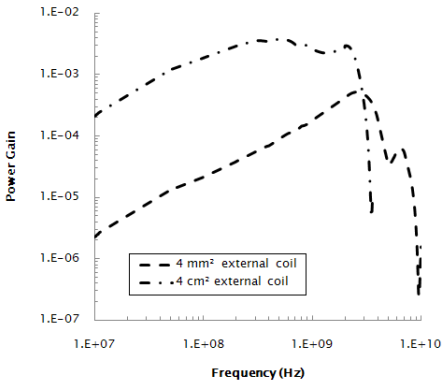

Fig. 12. With a bigger external coil ($4\ \mathrm{cm}^2$) the power gain increases and the optimal frequency slightly shifts in the sub-GHz range.

thus performing a *full-wave analysis*, the penetration depth is shown to be asymptotically independent with the frequency, until dielectric dispersion occurs at very high frequency, in the microwave range [64]. For this reason, an optimum frequency in the GHz range is assumed.

In this range of frequencies, to characterize a network in terms of lumped elements, as we have done in the previous paragraph, is difficult and in certain cases intractable. In microwave range, indeed, defining voltages and currents in a unique manner is not always possible. Moreover, the measurement of impedances and admittances, when possible, requires the use of short-circuits or open-circuits, not always easily realizable at high frequency. For these reasons, in the microwave and optical range a description of the networks by means of scattering parameters is usually preferred [65].

A brief introduction of the scattering parameters theory is given in the Appendix. By means of the theoretical elements introduced there, ref. [64] has simulated the performance of an inductive link consisting of two square coils with an area of $4\ \mathrm{mm}^2$. These coils are separated by a substrate of $1.5\ \mathrm{cm}$ (composed by air, $2\ \mathrm{mm}$ of skin, $1\ \mathrm{mm}$ of fat, $4\ \mathrm{mm}$ of muscle, $8\ \mathrm{mm}$ of skull and brain). The result obtained is reported in Fig. 11. The optimum frequency is located around 2.5 GHz, at least two orders of magnitude higher than the frequencies commonly used for the wireless power transmission. Moreover, this result has been validated by measurements using beef sirloin as substrate. The value of power gain is obtained by assuming simultaneous conjugate matching. The use of such range of frequencies would enable the realization of considerable smaller implantable coils, a higher data transmission rate and a better tolerance to misalignments between coils.

Our simulations, using the same setup as in [64], have confirmed that result. The electrical parameters of the human tissues have been calculated using the 4-terms Cole-Cole relaxation model [66]. The tool used to perform the simulations is the Agilent Momentum.

Other works [67] have shown an increase of the power gain, together with a shift of the optimal frequency in the sub-GHz range, where the area of the external coil is increased up to $4\ \mathrm{cm}^2$. The optimum frequency is still two orders of magnitude higher than the frequencies commonly used. Our simulations, reported in Fig. 12, confirm that behavior where a $4\ \mathrm{cm}^2$ external coil is used. These coils are electrically large at very high frequencies in the GHz range, thus resonance effects afflict the simulations with a sort of ripples in the high part of the simulation range.

Any kind of biomedical measurement performed by implanted devices requires a careful analysis of the implantation site. Measurements of biochemical species normally present into the muscles of the limbs, such as the lactate, can be performed by devices implanted into the legs or the arms. Moreover, sensors dedicated to monitor the neural activity must be placed near the brain. Finally, devices implanted into the wrist can easily detect the heart rate. Thus, different implantation sites have been tested, maintaining constant the area of the external coil at $4\ \mathrm{cm}^2$. The individuation of the sites and the definition of their geometries have been possible thanks to the Visible Human Project, implementing 3D real-time navigation into the human body [68]. The results of such simulations are reported in Fig. 13. The optimum frequency still remains in the sub-GHz range, while the absolute value of the power gain noticeably changes with the implantation depth.

To conclude the section dedicated to the high frequency inductive links, we report an example of implantable chip exploiting high frequency power transmission [69]. The working frequency is $915\ \mathrm{MHz}$ and it can deliver a maximum power of $140\ \mu\mathrm{W}$ at $1.2\ \mathrm{V}$, sending $0.25\ \mathrm{W}$ through $15\ \mathrm{mm}$ of tissue. The implanted coil has an area of $4\ \mathrm{mm}^2$, while the transmitting coil has an area of $4\ \mathrm{cm}^2$.

C. Specific Absorption Rate

An important parameter to be considered, when the power source is close to the body, is the *Specific Absorption Rate* (SAR) of the tissues:

$$\mathrm{SAR} = \frac{\sigma |\mathbf{E}|^2}{\rho}\ , \tag{17}$$

where σ and ρ are the conductivity and the density of the involved tissues, respectively, and $|\mathbf{E}|^2$ is the norm of the

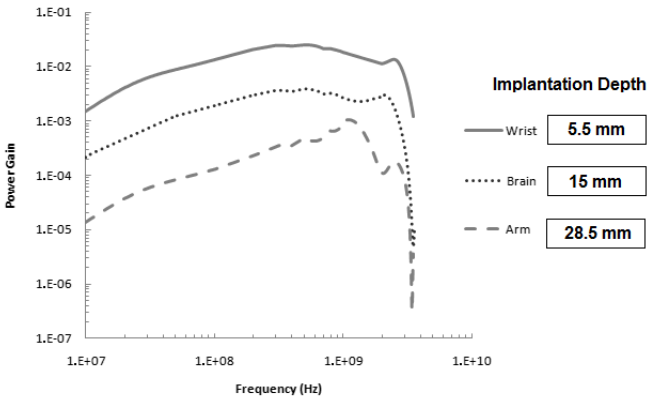

Fig. 13. Power gain obtained with a $4\ \mathrm{mm}^2$ receiving coil implanted in different parts of the body, where an external $4\ \mathrm{cm}^2$ transmitting coil is used. Power gain changes noticeably with the implantation depth, reported in the legend.

incident electric field. The SAR value, measured in $\mathrm{W/kg}$, determines the quantity of power absorbed by the tissues and is strictly related with their temperature increase. The SAR is usually calculated as an average over a region of $1\ \mathrm{g}$ or $10\ \mathrm{g}$ of tissue, depending on the national laws.

In the IEEE guideline [70], the SAR limits for a general public exposure are $4\ \mathrm{W/kg}$ for any $10\ \mathrm{g}$ of tissue of hands, wrists, feet and ankles, $1.6\ \mathrm{W/kg}$ for any $1\ \mathrm{g}$ of any other tissue. In the ICNIRP guideline [71], the SAR limits for a general public exposure are $2\ \mathrm{W/kg}$ for any $10\ \mathrm{g}$ of head and trunk, $4\ \mathrm{W/kg}$ for any $10\ \mathrm{g}$ of the limbs.

In ref. [72] a large number of cases where people were daily subjected to microwave fields with densities in the order of few $\mathrm{mW/cm^2}$ have been analyzed, without finding any significant health implication. In addition, it reports the trend of SAR on humans with respect to the frequency, when an incident field of $1\ \mathrm{mW/cm^2}$ is applied. The maximum absorption is around $70\ \mathrm{MHz}$, where SAR is equal to $0.225\ \mathrm{W/kg}$. At higher frequencies, around $2.45\ \mathrm{GHz}$, SAR is one order of magnitude smaller, being equal to $0.028\ \mathrm{W/kg}$. This value is comparable with that obtained around $20\ \mathrm{MHz}$, where SAR is equal to $0.015\ \mathrm{W/kg}$.

Recent studies have focused on the neurological effects of microwaves. The head has become the primary focus due to the wide use of electronic devices for mobile communication. With certain kinds of mobile phones, a maximum SAR of $3.72\ \mathrm{W/kg}$, averaged over $1\ \mathrm{g}$ of tissues of the head, can be reached at $900\ \mathrm{MHz}$ while the mobile phone is transmitting $600\ \mathrm{mW}$ [73]. If averaged over $10\ \mathrm{g}$ of tissues, the SAR can be $1.99\ \mathrm{W/kg}$. The increase of temperature of the head tissues is included in the range between $0.22\ ^\circ\mathrm{C}$ and $0.43\ ^\circ\mathrm{C}$. These measurements have been performed with a radiated power of $600\ \mathrm{mW}$. Ref. [74] found no positive evidence of risk to the health or the brain related to pulsed or continuous exposure to microwave having power levels typical of GSM communication, such as the ones previously reported.

D. Comparison of the Solutions

To recap, in Table II a summary of some works that exploit inductive links to power implantable devices is reported. For each of these, some of the key parameters have been extracted and reported in the table, to enable a fast comparison.

In contrast to other harvesting techniques presented before, inductive links are able to deliver a noticeable amount of power (order of mW) while occupying a relatively small area. Furthermore, power can be transferred wirelessly through the body tissues without any physical link that could cause infections or discomfort.

The distance between the coils is in the order of millimeters, ranging from $5\ \mathrm{mm}$ to $205\ \mathrm{mm}$. Most of the works presented in Table II perform a data communication between the external devices and the implanted sensors, with data rates up to few hundreds kbps. Finally, all the works reported in Table II use frequencies in the order of few MHz with the exception of the last one, where a frequency in the GHz range is used. The amount of power delivered by this last solution and its efficiency are noticeably smaller than the others, but they have been obtained using the smallest implanted coil among the others. Moreover, the use of a high frequency carrier could allow a higher data rate between the external devices and the implanted sensors.

IV. Conclusions

The field of implantable biosensors is attracting an increasing interest by offering wide applications for the future medicine. In this paper, we have analyzed some of the most popular techniques used for the design of implantable biosensors to harvest energy from the ambient and to remotely transmit it. For each technique, we have listed the advantages and the possible drawbacks. A special emphasis has been placed to the inductive links, able to deliver power wirelessly through the tissues and to perform bidirectional data communication with the implanted devices. Additionally, high frequency inductive links have been considered, showing the solutions presented in the literature and reporting the results returned by the simulations.

To summarize, in Table III have been listed the different solutions cited in the paper to enable a fast comparison among the different techniques described. For each example the returned power, the advantages, and the drawbacks are listed. By the examples reported in this table, inductive links seem to deliver the highest power levels. Moreover, the absence of moving parts together with the possibility to achieve bidirectional data communication without any implanted RF transmitter, make these technique particularly suitable to power implanted devices.

High frequency inductive links can achieve higher data rates and exhibit better tolerance to misalignments as compared to the low frequency solutions. Moreover, they support to realize implantable coils with an extremely low form factor as compared with other solutions exploiting inductive powering. The efficiency reached by this approach is however still lower than that obtained by classical approaches operating in the MHz range.

TABLE II
IMPLANTABLE DEVICES EXPLOITING INDUCTIVE LINKS FOR WIRELESS POWER TRANSMISSION.

Ref.	Coil Area ($\lambda = 10\ \mathrm{mm}^2$)	Coil Thickness ($\sigma = 1\ \mathrm{mm}$)	Carrier Frequency	Data Transmission	Bit Rate	Power Consumption	Efficiency	Distance	Measurement Site	Target Site
[52]	Tx: 7.8 λ Rx: 1.7 λ	Tx: 2 σ Rx: 2.5 σ	4 MHz	Downlink: PWM-ASK Uplink: LSK	Uplink: 125 kbps	90 mW *(a)*		5 mm	Air	Neural Recording System
[53]	Tx: 196 λ Rx: 31.4 λ	Tx: 9.5 σ Rx: 5 σ	4 MHz	Uplink: LSK	Uplink: $5 \div 10$ kbps	11 mW *(b)*		28 mm	Water Bearing Colloids	
[54]	Tx: 13200 λ Rx: 7.9 λ	Tx: 300 σ Rx: 13 σ	1 MHz			150 mW *(b)*	1 % (min.)	205 mm	PVC Barrel	Stomach
[55]	Rx: 10 λ	Rx: 0.035 σ	1 MHz			10 mW *(b)*	18.9% (max.)	5 mm	Air	Cerebral Cortex
[56]	Tx: 283 λ Rx: 31.4 λ		0.7 MHz	Downlink: ASK Uplink: LSK	Downlink: 60 kbps Uplink: 60 kbps	50 mW *(b)*	36% (max.)	30 mm		
[57]	Tx: 31.4 λ Rx: 7.9 λ		10 MHz	Downlink: ASK Uplink: BPSK	Downlink: 120 kbps Uplink: 234 kbps	≈ 22.5 mW in vitro *(b)* ≈ 19 mW in vivo *(b)*		15 mm	Rabbit	Muscle
[58]	Tx: 196.3 λ Rx: 3.5 λ	Tx: 5 σ Rx: 1.9 σ	5 MHz	Downlink: OOK	Downlink: 100 kbps	$\approx 5 \div 10$ mW *(a)*		40 mm		Neural Stimulator
[59]	Rx: 112.5 λ	Rx: 10 σ	6.78 MHz	Downlink: OOK Uplink: LSK	Uplink: 200 kbps	120 mW *(a)*	20% (min)	25 mm	Dog Shoulder	Muscular Stimulator
[60]	Tx: 152 λ Rx: 3.2 λ	Rx: 1 σ	13.56 MHz	Uplink: LSK		0.198 mW *(b)*		40 mm		Subcutaneous Tissue
[69]	Tx: 40 λ Rx: 0.4 λ	Tx: 0.038 σ Rx: 0.038 σ	915 MHz			0.14 mW *(b)*	0.06% (max)	15 mm	Bovine Muscle	

(a) Power consumed by the implantable sensor.
(b) Power effectively supplied by the inductive link.

TABLE III
COMPARISON BETWEEN THE DIFFERENT HARVESTING TECHNIQUES.

Technique	Ref.	Returned Power	Advantages	Drawbacks
Kinetic	[13]	$\simeq 44\ \mu$W		Large dimension ($\simeq 7\ \mathrm{cm}^2$).
	[14]	58 μW		
	[15]	80 μW	Non resonant.	
	[16]	60 μW	Dimension ($\leq 1\ \mathrm{cm}^2$).	Performance can decrease when packaged.
	[17]	40 μW		
Thermoelectric	[27]	22.5 μW		Low voltage drop.
	[28]	1.5 μW		
	[29]	1 μW		
	[30]	30 μW		
Fuel Cells	[35]	50 $\mu\mathrm{W/cm}^2$		*In vitro*.
	[36]	2.2 $\mu\mathrm{W/cm}^2$	*In vivo*.	
	[37]	430 $\mu\mathrm{W/cm}^2$	High power density.	Short lifetime.
Infrared Radiation	[41]	$\simeq 4$ mW	High power.	Dimension increases when thick tissues are used (10 cm^2 for 2 mm of human skin).
Low Frequency Magnetic Field	[43]	up to 3.1 W	Extremely high power over a big distance (up to 2 cm).	Extremely big dimension (10 cm^3). Moving parts need to be lubricated and substituted when worn out.
Inductive Links	[53]	11 mW	High quantity of power. Data transmission (except [54, 55]).	
	[54]	150 mW		
	[55]	10 mW		
	[56]	50 mW		
	[57]	up to 22.5 mW		
	[69]	0.14 mW	Extremely small dimension. Possibility of high data rate.	Extremely low efficiency. High transmitted power (0.25 W).

APPENDIX

We append here a brief introduction to the theory of scattering parameters. As introduced in Section 3, at high frequencies, such as in the microwave range, can be difficult or even impossible to describe a circuit by using voltages and currents. Moreover, the measurement of impedances and admittances may require the use of short-circuits or open-circuits that are not always easy to realize at high frequency. Consequently, in the microwave and optical range a description of the networks by means of scattering parameters is usually preferred [65].

Referring to Fig. 14, each voltage and current of a two-port network can be divided into two components, one incident and the other reflected,

$$\begin{cases} V_n = V_n^+ + V_n^- \ , & \text{(18a)} \\ I_n = \dfrac{1}{Z_{0n}}(V_n^+ - V_n^-) \ , & \text{(18b)} \end{cases}$$

where V_n^+ and V_n^- are the incident and the reflected components, respectively, and Z_{0n} is the characteristic impedance of port n. Both voltages and currents are represented as complex vectors.

When the various ports of a network present different characteristic impedances, it has sense to normalize the components just introduced:

$$\begin{cases} a_n = \dfrac{1}{\sqrt{Z_{0n}}} V_n^+ \ , & \text{(19a)} \\ b_n = \dfrac{1}{\sqrt{Z_{0n}}} V_n^- \ . & \text{(19b)} \end{cases}$$

Thus, it is possible to rewrite the voltages and the currents of the network as

$$\begin{cases} V_n = \sqrt{Z_{0n}}(a_n + b_n) \ , & \text{(20a)} \\ I_n = \dfrac{1}{\sqrt{Z_{0n}}}(a_n - b_n) \ , & \text{(20b)} \end{cases}$$

where n is still referred to the port. It is now possible to introduce the generalized scattering matrix S

$$\begin{cases} b_1 = S_{11}a_1 + S_{12}a_2 \ , & \text{(21a)} \\ b_2 = S_{21}a_1 + S_{22}a_2 \ , & \text{(21b)} \end{cases}$$

where the generic element S_{ij} can be expressed as

$$S_{ij} = \left.\frac{b_i}{a_j}\right|_{a_k=0 \text{ for } k\neq j} \ . \qquad \text{(22)}$$

In most of the practical situations, the characteristic impedance is the same for all the ports of a network. In that case, its value is indicated as Z_0 and is called characteristic impedance of the network. Consequently, the normalization factor will be the same for all the ports and equal to $\sqrt{Z_0}$.

The use of a normalization factor involves some advantages. First, differently from V_n and I_n, the normalized factors a_n and b_n are directly related to the power flow, being $|a_n|^2$ and $|b_n|^2$ the power incident and reflected at port n.

The coefficients indicated with the greek letter Γ in Fig. 14 are called reflection coefficients and describe the ratio of the amplitude of the reflected wave to the amplitude of the incident wave. With relation to Fig. 14, these coefficients can be written as

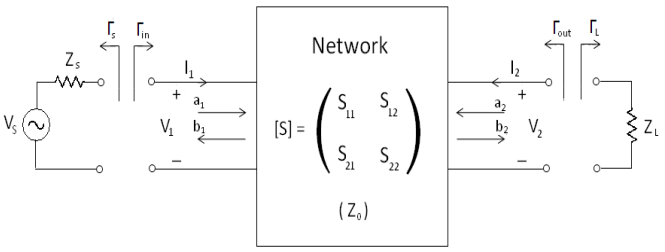

Fig. 14. Schematic description of a two-ports network by means of the scattering parameters.

$$\begin{cases} \Gamma_S = \dfrac{Z_S - Z_0}{Z_S + Z_0} \ , & \text{(23a)} \\ \Gamma_L = \dfrac{Z_L - Z_0}{Z_L + Z_0} \ , & \text{(23b)} \end{cases}$$

where Z_S and Z_L are the source and load impedances, respectively.

The signals involved in the two-ports network reported in Fig. 14 can be expressed by means of a signal flow graph, as that shown in Fig. 15. Incident wave generated by the source V_S is indicated as b_S and can be shown that $b_S = V_S \frac{\sqrt{Z_0}}{Z_S + Z_0}$.

Referring to Fig. 15, it is now possible to introduce the definitions of power gain:

$$\begin{cases} G_T \doteq \dfrac{P_d}{P_{avs}} \ , & \text{Transducer Power Gain} \quad \text{(24a)} \\ G \doteq \dfrac{P_d}{P_i} \ , & \text{Power Gain} \quad \text{(24b)} \\ G_A \doteq \dfrac{P_{avo}}{P_{avs}} \ , & \text{Available Gain} \quad \text{(24c)} \end{cases}$$

where P_{avs} is the power available from the source, P_i is the power at the input port of the network, P_{avo} is the power available at the output port of the network, and P_d is power delivered to the load. The different power gains can be rewritten as

$$\begin{cases} G_T = \dfrac{1 - |\Gamma_S|^2}{|1 - \Gamma_{in}\Gamma_S|^2} \cdot |S_{21}|^2 \cdot \dfrac{1 - |\Gamma_L|^2}{|1 - S_{22}\Gamma_L|^2} \ , & \text{(25a)} \\ G = \dfrac{1}{1 - |\Gamma_{in}|^2} \cdot |S_{21}|^2 \cdot \dfrac{1 - |\Gamma_L|^2}{|1 - S_{22}\Gamma_L|^2} \ , & \text{(25b)} \\ G_A = \dfrac{1 - |\Gamma_S|^2}{|1 - S_{11}\Gamma_S|^2} \cdot |S_{21}|^2 \cdot \dfrac{1}{1 - |\Gamma_{out}|^2} \ , & \text{(25c)} \end{cases}$$

where $\Gamma_{in} = S_{11} + \frac{S_{12}S_{21}\Gamma_L}{1 - S_{22}\Gamma_L}$ and $\Gamma_{out} = S_{22} + \frac{S_{12}S_{21}\Gamma_S}{1 - S_{11}\Gamma_S}$.

An important situation is when the input impedance and the output impedance of the network are conjugately matched to the source impedance and to the load impedance, respectively. In this case, named *simultaneous conjugate match*, the three definitions of power gain that we have reported assume the same maximum value.

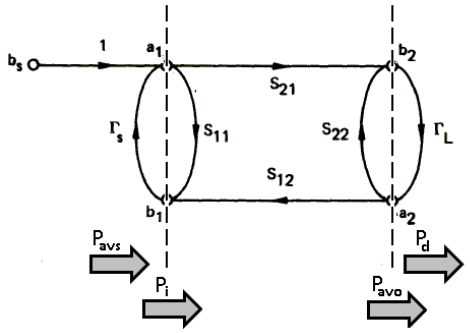

Fig. 15. Signal flow chart of a two-ports network.

Finally, it is useful to introduce the voltage gain at the ports of the network. By defining

$$\begin{cases} A_{11} \doteq \Gamma_{\mathrm{S}} S_{11} - 1 \ , & \text{(26a)} \\ A_{12} \doteq \Gamma_{\mathrm{S}} S_{12} \ , & \text{(26b)} \\ A_{21} \doteq \Gamma_{\mathrm{L}} S_{21} \ , & \text{(26c)} \\ A_{22} \doteq \Gamma_{\mathrm{L}} S_{22} - 1 \ , & \text{(26d)} \end{cases}$$

the voltage gain is equal to

$$A_{\mathrm{v}} = \frac{a_2 + b_2}{a_1 + b_1} = \frac{-A_{21} + (A_{22} S_{21} - S_{22} A_{21})}{A_{22} + (A_{22} S_{11} - S_{12} A_{21})} \ . \qquad (27)$$

With these theoretical elements a two ports network, such as an inductive link for remote powering, can be analyzed by the means of the scattering parameters. As previously mentioned, the description of a network by means of scattering parameters is always possible, while it is not always possible or convenient to use an approach exploiting lumped elements.

ACKNOWLEDGMENTS

J.O. thanks: J.Anders from EPFL and A.A.M. Perez from Agilent Technologies for the precious suggestions and the useful discussions about microwave networks and scattering parameters; K.M.Silay and Dr. C.Dehollain from EPFL for the advice on inductive links and their practical realization. The research work presented in this paper was funded by the i-IronIC project and by the NanoArch project. The NanoArch project is within the program ERC-2009, the i-IronIC project was financed with a grant from the Swiss Nano-Tera.ch initiative and evaluated by the Swiss National Science Foundation.

REFERENCES

[1] G. Buzsaki, "Large-scale Recording of Neuronal Ensembles," *Nature Neuroscience*, vol. 7, no. 5, pp. 446–451, May 2004.

[2] M. Nicolelis, D. Dimitrov, J. Carmena, R. Crist, G. Lehew, J. Kralik, and S. Wise, "Chronic, Multisite, Multielectrode Recordings in Macaque Monkeys," *Proceedings of the National Academy of Sciences of the United States of America*, vol. 100, no. 19, pp. 11 041–11 046, 2003.

[3] Z. Zumsteg, C. Kemere, S. O'Driscoll, G. Santhanam, R. Ahmed, K. Shenoy, and T. Meng, "Power Feasibility of Implantable Digital Spike-sorting Circuits for Neural Prosthetic Systems," *IEEE Transactions on Neural Systems and Rehabilitation Engineering*, vol. 13, no. 3, pp. 272–279, 2005.

[4] K. Wise, D. Anderson, J. Hetke, D. Kipke, and K. Najafi, "Wireless Implantable Microsystems: High-density Electronic Interfaces to the Nervous Systems," *Proceedings of the IEEE*, vol. 92, no. 1, pp. 76–97, Jan 2004.

[5] M. Carrozza, G. Cappiello, S. Micera, B. Edin, L. Beccai, and C. Cipriani, "Design of a Cybernetic Hand for Perception and Action," *Biological Cybernetics*, vol. 95, no. 6, pp. 629–644, Dec 2006.

[6] M. C. Frost and M. E. Meyerhoff, "Implantable Chemical Sensors for Real-time Clinical Monitoring: Progress and Challenges," *Current Opinion in Chemical Biology*, vol. 6, no. 5, pp. 633 – 641, 2002.

[7] G. Lazzi, "Thermal Effects of Bioimplants," *IEEE Engineering in Medicine and Biology Magazine*, vol. 24, no. 5, pp. 75–81, 2005.

[8] A. Du Pasquier, I. Plitz, S. Menocal, and G. Amatucci, "A Comparative Study of Li-ion Battery, Supercapacitor and Nonaqueous Asymmetric Hybrid Devices for Automotive Applications," *Journal of Power Sources*, vol. 115, no. 1, pp. 171–178, Mar 2003.

[9] Integrated Pressure Sensors for Medical Use. Fraunhofer Institute for Microelectronic Circuits and Systems. [Online]. Available: http://www.ims.fraunhofer.de/

[10] P. Mitcheson, E. Yeatman, G. Rao, A. Holmes, and T. Green, "Energy Harvesting from Human and Machine Motion for Wireless Electronic Devices," *Proceedings of the IEEE*, vol. 96, no. 9, pp. 1457–1486, 2008.

[11] European Patent Office Patent 0 326 313, 1989.

[12] M. Hayakawa, "A Study of the New Energy System for Quartz Watches (ii) - The Effective Circuit for the System," in *Congrès Européen de Chronométrie*, 1988.

[13] H. Goto, T. Sugiura, Y. Harada, and T. Kazui, "Feasibility of Using the Automatic Generating System for Quartz Watches as a Leadless Pacemaker Power Source," *Medical and Biological Engineering and Computing*, vol. 37, no. 1, pp. 377–380, Jan 1999.

[14] R. Tashiro, N. Kabei, K. Katayama, Y. Ishizuka, F. Tsuboi, and K. Tsuchiya, "Development of an Electrostatic Generator that Harnesses the Motion of a Living Body," *International Journal of Japanese Society of Mechanical Engineers*, vol. 43, pp. 916–922, 2000.

[15] P. Miao, P. Mitcheson, A. Holmes, E. Yeatman, T. Green, and B. Stark, "MEMS Inertial Power Generators for Biomedical Applications," *Microsystem Technologies*, vol. 12, no. 10-11, pp. 1079–1083, Sep 2006.

[16] R. Elfrink, T. M. Kamel, M. Goedbloed, S. Matova, D. Hohlfeld, Y. van Andel, and R. van Schaijk, "Vibration Energy Harvesting with Aluminum Nitride-based Piezoelectric Devices," *Journal of Micromechanics and Microengineering*, vol. 19, no. 9, p. 094005, 2009.

[17] M. Renaud, K. Karakaya, T. Sterken, P. Fiorini, C. V. Hoof, and R. Puers, "Fabrication, Modelling and Characterization of MEMS Piezoelectric Vibration Harvesters," *Sensors and Actuators A: Physical*, vol. 145-146, pp. 380 – 386, 2008.

[18] [Online]. Available: http://www.perpetuum.com/

[19] [Online]. Available: http://www.enocean.com/

[20] R. Vullers, R. van Schaijk, I. Doms, C. van Hoof, and R. Mertens, "Micropower Energy Harvesting," *Solid-State Electronics*, vol. 53, no. 7, pp. 684 – 693, 2009.

[21] V. Leonov, T. Torfs, P. Fiorini, and C. van Hoof, "Thermoelectric Converters of Human Warmth for Self-powered Wireless Sensor Nodes," *IEEE Sensors Journal*, vol. 7, no. 5, pp. 650–657, 2007.

[22] P. Wright. Energy Harvesting in the Human Body (Implantable Self-Powered Sensors). Presentation, BWRC Summer 2008 Retreat.

[23] P. Favrat, P. Deval, and M. Declercq, "A High-efficiency cmos Voltage Doubler," *IEEE Journal of Solid-State Circuits*, vol. 33, no. 3, pp. 410–416, Mar 1998.

[24] J. Dickson, "On-chip High-voltage Generation in nmos Integrated Circuits Using an Improved Voltage Multiplier Technique," *IEEE Journal of Solid-State Circuits*, vol. 11, no. 6, pp. 374–378, Jun 1976.

[25] J. Silva-Martinez, "A Switched Capacitor Double Voltage Generator," *Proceedings of the 37th Midwest Symposium on Circuits and Systems*, vol. 1, pp. 177–180, 1994.

[26] J. Wu and K. Chang, "Mos Charge Pumps for Low-voltage Operation," *IEEE Journal of Solid-State Circuits*, vol. 33, no. 4, pp. 592–597, Apr 1998.

[27] M. Kishi, H. Nemoto, T. Hamao, M. Yamamoto, S. Sudou, M. Mandai, and S. Yamamoto, "Micro Thermoelectric Modules and their Application to Wristwatches as an Energy Source," *18th International Conference on Thermoelectric*, pp. 301–307, 1999.

[28] I. Stark and M. Stordeur, "New Micro Thermoelectric Devices Based on Bismuth Telluride-Type Thin Solid Films," *18th International Conference on Thermoelectric*, pp. 465–472, 1999.

[29] M. Strasser, R. Aigner, C. Lauterbach, T. F. Sturm, M. Franosch, and G. Wachutka, "Micromachined CMOS Thermoelectric Generators as On-chip Power Supply," *Sensors and Actuators A: Physical*, vol. 114, no. 2-3, pp. 362 – 370, 2004.

[30] [Online]. Available: http://www.poweredbythermolife.com

[31] R. Ferrigno, A. Stroock, T. Clark, M. Mayer, and G. Whitesides, "Membraneless Vanadium Redox Fuel Cell Using Laminar Flow," *Journal of the American Chemical Society*, vol. 124, no. 44, pp. 12 930–12 931, Nov 2002.

[32] E. Choban, L. Markoski, A. Wieckowski, and P. Kenis, "Microfluidic Fuel Cell Based on Laminar Flow," *Journal of Power Sources*, vol. 128, no. 1, pp. 54–60, Mar 2004.

[33] S. Wolfson Jr, S. Gofberg, P. Prusiner, and L. Nanis, "The Bioautofuel Cell: a Device for Pacemaker Power from Direct Energy Conversion Consuming Autogenous Fuel," *Transactions - American Society for Artificial Internal Organs*, vol. 14, pp. 198–203, 1968.

[34] S. Kerzenmacher, J. Ducre, R. Zengerle, and F. von Stetten, "Energy Harvesting by Implantable Abiotically Catalyzed Glucose Fuel Cells," *Journal of Power Sources*, vol. 182, no. 1, pp. 1–17, Jul 2008.

[35] P. Malachesky, G. Holleck, F. McGovern, and R. Devarakonda, "Parametric Studies of Implantable Fuel Cell," *Proceedings of the 7th Intersociety Energy Conversion Engineering Conference*, pp. 727–732, 1972.

[36] R. Drake, B. Kusserow, S. Messinger, and S. Matsuda, "A Tissue Implantable Fuel Cell Power Supply," *ASAIO Journal*, vol. 16, no. 1, pp. 199–205, 1970.

[37] N. Mano, F. Mao, and A. Heller, "Characteristics of a Miniature Compartment-less Glucose-O_2 Biofuel Cell and its Operation in a Living Plant," *Journal of the American Chemical Society*, vol. 125, no. 21, pp. 6588–6594, May 2003.

[38] R. Bullen, T. Arnot, J. Lakeman, and F. Walsh, "Biofuel Cells and their Development," *Biosensors and Bioelectronics*, vol. 21, no. 11, pp. 2015 – 2045, 2006.

[39] J. Phirani and S. Basu, "Analyses of Fuel Utilization in Microfluidic Fuel Cell," *Journal of Power Sources*, vol. 175, no. 1, pp. 261–265, Jan 2008.

[40] K. Murakawa, M. Kobayashi, O. Nakamura, and S. Kawata, "A Wireless Near-infrared Energy System for Medical Implants," *Engineering in Medicine and Biology Magazine, IEEE*, vol. 18, no. 6, pp. 70 –72, nov.-dec. 1999.

[41] K. Goto, T. Nakagawa, O. Nakamura, and S. Kawata, "An Implantable Power Supply with an Optical Rechargeable Lithium Battery," *IEEE Transactions on Biomedical Engineering*, vol. 48, no. 7, pp. 830–833, 2001.

[42] T. Oshita and R. Calderhead, *Low Level Laser Therapy: A Practical Introduction*. New York: Wiley, 1988.

[43] S. Suzuki, T. Katane, H. Saotome, and O. Saito, "Electric Power-generating System Using Magnetic Coupling for Deeply Implanted Medical Electronic Devices," *IEEE Transactions on Magnetics*, vol. 38, pp. 3006–3008, 2002.

[44] S. Suzuki, T. Katane, H. Saotome, and O. Saito, "A Proposal of Electric Power Generating System for Implanted Medical Devices," *IEEE Transactions on Magnetics*, vol. 35, no. 5, pp. 3586 –3588, Sep 1999.

[45] E. Ngai, K. K. Moon, F. J. Riggins, and C. Y. Yi, "RFID Research: An Academic Literature Review (1995-2005) and Future Research Directions," *International Journal of Production Economics*, vol. 112, no. 2, pp. 510 – 520, 2008.

[46] Activa RC Recharging System 37751. Medtronic.

[47] R. Sarpeshkar, *Ultra Low Power Bioelectronics: Fundamentals, Biomedical Applications, and Bio-inspired Systems*. Cambridge University Press, 2010.

[48] K. Kalyanasundaram and M. Grätzel, "Artificial Photosynthesis: Biomimetic Approaches to Solar Energy Conversion and Storage," *Current Opinion in Biotechnology*, vol. 21, no. 3, pp. 298 – 310, 2010.

[49] I. McConnell, G. Li, and G. W. Brudvig, "Energy Conversion in Natural and Artificial Photosynthesis," *Chemistry & Biology*, vol. 17, no. 5, pp. 434 – 447, 2010.

[50] M. Katterle, V. I. Prokhorenko, A. R. Holzwarth, and A. Jesorka, "An artificial supramolecular photosynthetic unit," *Chemical Physics Letters*, vol. 447, no. 4-6, pp. 284 – 288, 2007.

[51] M. Grätzel, "Photoelectrochemical cells," *Nature*, vol. 414, no. 6861, pp. 338–344, 2001.

[52] T. Akin, K. Najafi, and R. Bradley, "A Wireless Implantable Multichannel Digital Neural Recording System for a Micromachined Sieve Electrode," *IEEE Journal of Solid-State Circuits*, vol. 33, no. 1, pp. 109 –118, Jan 1998.

[53] C. Sauer, M. Stanacevic, G. Cauwenberghs, and N. Thakor, "Power Harvesting and Telemetry in CMOS for Implanted Devices," *IEEE Transactions on Circuits and Systems I: Regular Papers*, vol. 52, no. 12, pp. 2605 – 2613, Dec 2005.

[54] B. Lenaerts and R. Puers, "An Inductive Power Link for a Wireless Endoscope," *Biosensors and Bioelectronics*, vol. 22, no. 7, pp. 1390 – 1395, 2007.

[55] K. Silay, D. Dondi, L. Larcher, M. Declercq, L. Benini, Y. Leblebici, and C. Dehollain, "Load Optimization of an Inductive Power Link for Remote Powering of Biomedical Implants," *Proceedings of the IEEE International Symposium on Circuits and Systems 2009 (ISCAS'09)*, pp. 533 –536, May 2009.

[56] M. Catrysse, B. Hermans, and R. Puers, "An Inductive Power System with Integrated Bi-directional Data-transmission," *Sensors and Actuators A: Physical*, vol. 115, no. 2-3, pp. 221 – 229, Sep 2004.

[57] J. Parramon, P. Doguet, D. Marin, M. Verleyssen, R. Munoz, L. Leija, and E. Valderrama, "ASIC-Based Batteryless Implantable Telemetry Microsystem for Recording Purposes," *Proceedings of the 19th Annual International Conference of the IEEE Engineering in Medicine and Biology Society*, vol. 5, pp. 2225 –2228, 1997.

[58] G. Gudnason, E. Bruun, and M. Haugland, "A Chip for an Implantable Neural Stimulator," *Analog Integrated Circuits and Signal Processing*, vol. 22, no. 1, pp. 81–89, 2000.

[59] B. Smith, Z. Tang, M. Johnson, S. Pourmehdi, M. Gazdik, J. Buckett, and P. Peckham, "An Externally Powered, Multichannel, Implantable Stimulator-Telemeter for Control of Paralyzed Muscle," *IEEE Transactions on Biomedical Engineering*, vol. 45, no. 4, pp. 463 –475, Apr 1998.

[60] M. Ahmadi and G. Jullien, "A Wireless-Implantable Microsystem for Continuous Blood Glucose Monitoring," *Biomedical Circuits and Systems, IEEE Transactions on*, vol. 3, no. 3, pp. 169 –180, jun. 2009.

[61] B. Lenaerts and R. Puers, *Omnidirectional Inductive Powering for Biomedical Implants*. Springer, 2009.

[62] N. Sokal, "Class-E RF Power Amplifiers," *QEX*, pp. 9–20, Jan/Feb 2001.

[63] M. Ghovanloo and K. Najafi, "A High Data Transfer Rate Frequency Shift Keying Demodulator Chip for the Wireless Biomedical Implants," *45th Midwest Symposium on Circuits and Systems (MWSCAS'02)*, vol. 3, pp. 433–436, 2002.

[64] A. Poon, S. O'Driscoll, and T. Meng, "Optimal Operating Frequency in Wireless Power Transmission for Implantable Devices," *Proceedings of the 29th Annual International Conference of the IEEE EMBS*, pp. 5673–5678, 2007.

[65] D. Pozar, *Microwave Engineering - Third Edition*. John Wiley & Sons, 2005.

[66] S. Gabriel, R. Lau, and C. Gabriel, "The Dielectric Properties of Biological Tissues: III. Parametric Models for the Dielectric Spectrum of Tissues," *Physics in Medicine and Biology*, vol. 41, pp. 2271–2293, 1996.

[67] A. Poon, S. O'Driscoll, and T. Meng, "Optimal Frequency for Wireless Power Transmission into Dispersive Tissue," *IEEE Transactions on Antennas and Propagation*, vol. 58, no. 5, pp. 1739–1750, 2010.

[68] [Online]. Available: http://visiblehuman.epfl.ch/

[69] A. Poon, S. O'Driscoll, and T. Meng, "A mm-sized Implantable Power Receiver with Adaptative Link Compensation," *Technical Digest of IEEE International Solid-State Circuits Conference*, vol. ser. Paper 17.5, 2009.

[70] *IEEE Standard for Safety Levels with Respect to Human Exposure to Radio Frequency Electromagnetic Fields, 3 kHz to 3 Ghz*, IEEE Std. C95-1, 1999.

[71] *Guidelines for Limiting Exposure to Time-Varying Electric, Magnetic and Electromagnetic Fields (Up to 300 GHz)*, International Commission on Non-Ionizing Radation Protection Std.

[72] S. Michaelson, "Health Implications of Exposure to Radiofrequency/Microwave Energies," *British Journal of Industrial Medicine*, vol. 39, pp. 105–119, 1982.

[73] P. Bernardi, M. Cavagnaro, S. Pisa, and E. Piuzzi, "Specific Absorption Rate and Temperature Increases in the Head of a Cellular-phone User," *Microwave Theory and Techniques, IEEE Transactions on*, vol. 48, no. 7, pp. 1118 –1126, jul. 2000.

[74] D. Hermann and K. Hossmann, "Neurological effects of microwave exposure related to mobile communication," *Journal of the Neurological Sciences*, vol. 152, no. 1, pp. 1 – 14, 1997.